Chemical Science

ROYAL SOCIETY OF CHEMISTRY

EDGE ARTICLE

View Article Online
View Journal

Cite this: DOI: 10.1039/d5sc08499g

All publication charges for this article have been paid for by the Royal Society of Chemistry

Rotational symmetry dication assembling ferroelectric, thermochromic and circularly polarized luminescent multifunctional manganese(II) bromide hybrid

Jiayi Yuan,[a] Yu Xu,[a] Lu Zhai, *[a] Shan-Shan Hei,[a] Jianyi Huang,[b] Weihua Ning, *[b] Hong-Ling Cai *[c] and Xiao-Ming Ren *[a]

Received 3rd November 2025
Accepted 12th January 2026

DOI: 10.1039/d5sc08499g

rsc.li/chemical-science

Noncentrosymmetric (NCS) structure crystalline materials exhibit a range of high-tech applications; however, the controllable synthesis of NCS materials using achiral molecular building blocks remains a great challenge. Herein, we present a crystal engineering strategy for constructing NCS multifunctional materials. We designed 1,4-diazabicyclo[2.2.2]octane (DABCO) derivative dication, which adopts a chiral conformation, despite lacking chiral carbon atoms. These dications were assembled with tetrahedral $[MnX_4]^{2-}$ anions to induce asymmetry into the structure. The high directionality H···X interactions between the anions and cations induce and stabilize NCS ion-pair structures, leading to NCS crystallization. We successfully obtained an NCS hybrid crystal, [H–Pr-DABCO]$MnBr_4$ (where H and Pr represent proton and *normal*-propyl groups, respectively). This compound crystallizes in a polar space group $P2_1$ at room temperature and undergoes a reversible phase transition between two polar phases. This chiral-polar hybrid crystal integrates multiple functionalities, including switchable dielectric behavior, reversible thermochromism, second-order nonlinear optical activity, ferroelectricity, and circularly polarized luminescence. Moreover, the material exhibits a notable spontaneous polarization of 21.5 μC cm^{-2}, close to that of the typical inorganic ferroelectric $BaTiO_3$. This work elucidates a design strategy for constructing multifunctional materials, highlighting their potential for application in advanced devices.

Introduction

Crystalline materials with noncentrosymmetric (NCS) structures exhibit a range of valuable physical properties, such as second-order nonlinear optics,[1] circularly polarized luminescence (CPL),[2] pyroelectricity,[3] piezoelectricity,[4] ferroelectricity,[5] and multiferroicity.[6] These properties make them critical for high-tech applications, including sensors,[7] actuators,[8] information storage and processing,[9] and encryption and anti-counterfeiting.[10] Despite significant achievements in the molecular design and crystal engineering of NCS materials, the controllable synthesis of these structures remains a major challenge.

A common strategy for obtaining NCS crystals involves introducing chiral groups into organic components of organic or hybrid materials to promote crystallization in NCS space groups.[11–14] However, this approach is often limited by the cumbersome synthesis of the required chiral molecules, which typically involves complex conditions and expensive reagents. In contrast, achieving NCS structures from achiral molecular building blocks presents an appealing alternative,[15] yet it faces considerable challenges due to the inherent tendency of achiral molecules to pack into centrosymmetric arrangements.[16]

Significant research efforts over the past two decades have been devoted to overcoming this challenge. For instance, Lin and co-workers[17] proposed a design principle for synthesizing acentric metal–organic frameworks (MOFs) for second-order nonlinear optics. Their approach involved assembling tetrahedral metal nodes with unsymmetrical linkers to form diamondoid NCS structures. Jornet-Mollá *et al.*[18] developed a predictive synthetic strategy based on the high directionality of hydrogen bonds. Using this method, they successfully obtained a ferroelectric spin-crossover complex, $[Fe(bpp)_2](isonic)_2 \cdot 2H_2O$. In this structure, bpp (2,6-bis(pyrazol-3-yl) pyridine) acts as a four-fold noncentrosymmetric hydrogen-bond donor, while the isonicotinate anion (isonic) serves as a dissymmetric hydrogen-bond acceptor. Additionally, Xiong and coworkers introduced a novel 'pseudo-spheric strategy' for

[a]State Key Laboratory of Materials-Oriented Chemical Engineering and College of Chemistry and Molecular Engineering, Nanjing Tech University, Nanjing 211816, P. R. China. E-mail: zhailu@njtech.edu.cn; xmren@njtech.edu.cn

[b]Institute of Functional Nano & Soft Materials (FUNSOM), Joint International Research Laboratory of Carbon-Based Functional Materials and Devices, Soochow University, Suzhou 215123, P. R. China. E-mail: whning@suda.edu.cn

[c]National Laboratory of Solid-State Microstructures, Collaborative Innovation Center of Advanced Microstructures, School of Physics, Nanjing University, Nanjing 210093, P. R. China. E-mail: hlcai@nju.edu.cn

designing inorganic–organic hybrid ferroelectric crystals. This approach involves introducing substituents to create globular-shaped organic ammonium cations in the organic components that undergo symmetry breaking, thereby facilitating the formation of polar crystalline structures.[19–21]

In a previous study, we proposed a design strategy for preparing chiral hybrid crystals *via* the self-assembly of achiral molecular building blocks.[22] Specifically, we selected 1,4-diazabicyclo[2.2.2]octane (DABCO) derivative dication. While these cations lack chiral carbon atoms, they adopt a chiral conformation. We employed them as countercations for the tetrahedral $[MnBr_4]^{2-}$ anion, hypothesizing that the high directionality H···X interactions between the anion and cations could induce and stabilize noncentrosymmetric (NCS) structures. This strategy successfully yielded an NCS hybrid crystal, [Me–Pr-DABCO]$MnBr_4$ (where Me and Pr represent methyl and *normal*-propyl groups, respectively). The compound crystallizes in the chiral space group $P2_12_12_1$ and exhibits an excellent CPL response, achieving a record-high figure of merit among reported Mn^{2+}-based CPL materials.

Building on this strategy, we have successfully prepared a new hybrid compound, [H–Pr-DABCO]$MnBr_4$ (**1**, H–Pr-DABCO = 1-*normal*-propyl-1,4-diazabicyclo-[2.2.2]octan-1-ium). Compound **1** crystallizes in the polar space group $P2_1$ at room temperature and remarkably integrates multifunctionalities, including reversible phase transition between two polar phases, switchable dielectric behavior, reversible thermochromism, second-order nonlinear optical activity, ferroelectricity, and CPL. This work demonstrates a promising pathway for designing a new class of multifunctional NCS materials.

Results and discussion

Crystal growth and characterization of [H–Pr-DABCO]$MnBr_4$ (1)

Dark-yellow single crystals of **1** were prepared *via* a solvothermal reaction of $MnBr_2 \cdot H_2O$ and [H–Pr-DABCO]Br in a 1 : 2 molar ratio, using HBr and isopropanol as solvents. The resulting mixture was then allowed to evaporate in air for three days (Fig. S1, SI). Detailed experimental procedures are provided in the SI. Elemental microanalysis (C, H, N) and powder X-ray diffraction (PXRD) confirmed the high chemical and phase purity of the polycrystalline samples (Fig. S2). Thermogravimetric analysis indicated that the crystalline sample remains stable up to 565 K under a nitrogen atmosphere (Fig. S3a). Differential scanning calorimetry (DSC) revealed a pair of reversible thermal peaks centered at 438 K (endothermic) and 389 K (exothermic) during the first heating–cooling cycle, showing a large thermal hysteresis of 49 K (Fig. S3b). In subsequent cycles, the endothermic peak shifted to 428 K, a 10 K decrease likely resulting from an annealing process that eliminated crystal defects, leading to a more stable state.

Crystal structures in low- and high-temperature phases

To understand the phase transition, the crystal structures of **1** were determined at 293 K (low-temperature phase, LTP) and 438 K (high-temperature phase, HTP) on the same single crystal using X-ray diffraction (Table S1).

Crystal structure in LTP. Compound **1** in its LTP crystallizes in the monoclinic polar space group $P2_1$ (point group $C2$) with the unit cell parameters $a = 14.2814(11)$ Å, $b = 13.6741(9)$ Å, $c = 14.3160(16)$ Å, and $\beta = 119.883(2)°$. Notably, the a- and c-axes are of remarkably similar length, and the β angle is very close to 120°. This combination of metrics suggests a structure with pseudo-symmetry that is metrically similar to a hexagonal or trigonal system. The asymmetric unit contains three distinct $[H–Pr-DABCO]^{2+}$ cations and three different $[MnBr_4]^{2-}$ anions (Fig. 1a). Within the $[MnBr_4]^{2-}$ tetrahedra, the Mn–Br bond lengths range from 2.465(9) to 2.547(9) Å, and the Br–Mn–Br angles range from 104.1(3)° to 115.6(3)° (Fig. S4 and Table S2). The Mn^{2+} centers of adjacent tetrahedra are separated by distances ranging from 6.803 Å (shortest) to 10.967 Å (longest; Fig. 1b).

Viewing the packing along the b-axis reveals that the $[MnBr_4]^{2-}$ tetrahedra are fully separated by the $[H–Pr-DABCO]^{2+}$ cations (Fig. 1c). The neighboring cations align in a head-to-head manner along three different directions: [0 1 0], [0 0 1], and [1 1 0]. The entire structure is stabilized by an extensive hydrogen-bonding network, including N–H···Br and C–H···Br (Fig. S5, S6 and Table S3).

Crystal structure in HTP. Upon transition to the HTP, the space group changes from chiral $P2_1$ to the acentric space group $P3c1$, with cell parameters of $a = b = 14.4907(16)$ Å, $c = 13.6423(18)$ Å. The a-, b- and c-axes in the HTP correspond sequentially to the c-, a- and b-axes in the LTP. Compared to the LTP, the c-axis contracts slightly, while the a- and b-axes undergo a small expansion in the HTP. The asymmetric unit contains one two-fold disordered $[H–Pr-DABCO]^{2+}$ cation (Fig. 1d), three crystallographically independent Mn^{2+} ions (Mn1–Mn3), and six Br ions (Br1–Br6), each with a site occupancy of 1/3. The $[MnBr_4]^{2-}$ tetrahedra in the HTP are less distorted than those in the LTP, as evidenced by more regular Mn–Br bond lengths [2.469(10)–2.549(12) Å] and Br–Mn–Br angles [105.7(2)–113.0(2)°]. The nearest Mn···Mn distance is 6.821 Å, which is slightly longer than in the LTP due to the

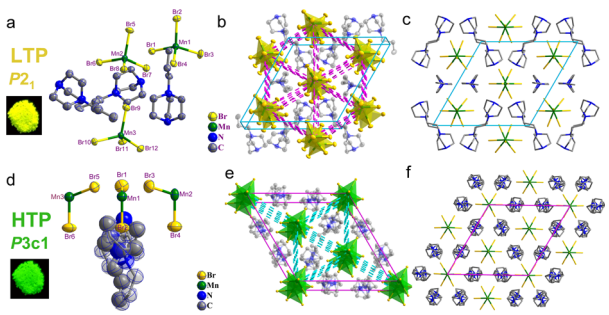

Fig. 1 (a) Asymmetric unit, (b) the illustration of Mn···Mn distances, and (c) packing diagram viewed along the b-axis of **1** at 293 K (LTP). (d) Asymmetric unit, (e) the illustration of Mn···Mn distances, and (f) packing diagram viewed along the c-axis of **1** at 438 K (HTP). In these structure plots, hydrogen atoms are omitted for clarity, and the thermal ellipsoids are at the 50% probability level.

overall lattice expansion (Fig. 1e). Although the packing diagram viewed along the *c*-axis in the HTP is analogous to that viewed along the *b*-axis in the LTP (Fig. 1f), key differences are observed: (1) in the LTP, adjacent cations align in a head-to-head manner along three distinct directions, whereas in the HTP, this alignment is reduced to a single direction, [0 0 1]. (2) The Mn^{2+} ions within a tetrahedron reorganize from a non-collinear arrangement (LTP) to a collinear one (HTP) (Fig. S7). These structural changes indicate that the phase transition involves a rotational motion of some cations and a concomitant displacement of the Mn^{2+} ions.

In hybrid materials, the coordination environment of the Mn^{2+} ion directly influences their optical properties. In both the LTP and HTP, there are three inequivalent $[MnBr_4]^{2-}$ tetrahedra. The Mn–Br bond lengths (d_{Mn-Br}) are 2.465(9)–2.547(9) Å for Mn1, 2.480(8)–2.518(8) Å for Mn2, and 2.509(8)–2.530(8) Å for Mn3 in the LTP. In the HTP, 2.494(4) and 2.494(10) Å for Mn1, 2.484(4) and 2.549(12) Å for Mn2, and 2.492(4) and 2.469(10) Å for Mn3 (Fig. S5). The disparity of bond lengths within the tetrahedra in both phases is attributed to the variations in C–H···Br/N–H···Br hydrogen bonding interactions between the Br atoms in the anions and the organic cations. This is due to a dense, closely packed hydrogen-bonding network formed between the organic cations and inorganic anions (Fig. S6). Particularly, there are two different H-bonding interactions (C–H···Br/N–H···Br) between $[Mn_1Br_4]^{2-}$ tetrahedra and organic cations in the LTP. The donor–acceptor (C···Br/N···Br) distances range from 2.648 to 3.200 Å in the LTP and from 2.623 to 3.190 Å in the HTP (Tables S3 and S4).

To quantify the tetrahedral distortion, we calculated the bond length distortion parameter (Δd) and the bond angle variance (σ^2) for the $[MnBr_4]^{2-}$ tetrahedra using the following equations:[23]

$$\Delta d = \frac{1}{4}\sum_{n=1}^{4}\left(\frac{d_n - d}{d}\right)^2 \quad (1)$$

$$\sigma^2 = \frac{1}{5}\sum_{i=1}^{6}(\theta_i - 109.47^\circ)^2 \quad (2)$$

In eqn (1), Δd is the difference in bond lengths, while d and d_n denote the mean and the individual Mn–Br bond length. In eqn (2), θ_i is the individual Br–Mn–Br angles and σ^2 denotes the variance in the tetrahedral bond angles. The calculated Δd and σ^2 values for each tetrahedron are listed in Table S5. The Δd values ($\times 10^5$) for Mn1, Mn2, and Mn3 are 16.48, 3.78, and 1.09 in the LTP, and 0.016, 16.68, and 0.64 in the HTP, respectively. The σ^2 values are 28.95, 14.95, and 13.31 for the LTP, and 0.027, 16.00, and 1.32 for the HTP, respectively. These results imply that the overall tetrahedral distortion decreases in the HTP. We therefore propose that the structural distortions of the $[MnBr_4]^{2-}$ units in both phases predominantly dictate their emission properties, with σ^2 being a key factor in determining structural asymmetry.[24]

Given that structural distortion is closely associated with intermolecular forces, we analyzed the interactions between the $[MnBr_4]^{2-}$ anions and organic cations in both phases using Hirshfeld surface analysis and 2D fingerprint plots.[25] The surfaces are colored red and blue, with red areas indicating strong intermolecular repulsive interactions. In the LTP, H···Br interactions account for approximately 50% of the total interactions (Fig. S10), compared to only 3.6% in the HTP (Fig. S11). This suggests the presence of stronger intermolecular interactions between the anions and cations in the LTP than in the HTP, which accounts for the much lower σ^2 value of HTP compared to that of LTP. The strong H···Br interactions in the LTP result in the heavy tetrahedral distortion of $[MnBr_4]^{2-}$ anions.

We further verified the structural phase transition using variable-temperature powder X-ray diffraction (VT-PXRD). As shown in Fig. S12, the PXRD patterns collected at 293 K and 438 K match well with their respective simulated patterns and are similar to each other. This is consistent with their very similar unit cell parameters. While most diffraction peaks remain nearly unchanged in position and intensity with increasing temperature, certain peaks exhibit obvious shifts. For example, the peaks in the region indicated by the purple dashed line, which correspond to the (3 0 0), (3 0 2), and (4 −2 1) crystallographic planes of the high-temperature phase (HTP), shift significantly. Furthermore, when the sample was cooled back to room temperature, the PXRD pattern reverted to that of the original sample, demonstrating the dynamics of anions and cations during the heating and cooling process and the reversibility of the phase transition.

Switchable dielectric, nonlinear optical and ferroelectricity properties

Crystal structure analysis revealed that the phase transition involves the rotational motion of part of the cationic moieties and a simultaneous displacement of Mn^{2+} ions within the lattice. These synergistic motions are likely responsible for the observed variation in dielectric permittivity. As shown in Fig. 2a, the temperature-dependent real part (ε') of the dielectric permittivity exhibits a step-like anomaly around 440 K, a temperature close to the endothermic peak observed in DSC. This anomaly in the ε' *vs.* T plot is attributed to dipole orientational dynamics[26] resulting from the structural phase transition. Fig. 2b shows the reversible switching of the dielectric permittivity between high-dielectric permittivity ("ON") and low-dielectric permittivity ("OFF") states at 1 kHz for **1**. The switch ratio ($\varepsilon'_{high}/\varepsilon'_{low}$) near the phase transition temperature is approximately 3 over multiple cycles, indicating good stability and cyclability.

Since **1** crystallizes in a non-centrosymmetric space group, we conducted second-harmonic generation (SHG) measurements on single crystals. At room temperature, the SHG intensity is approximately 0.88 times that of potassium dihydrogen phosphate (KDP) (Fig. 2c). Furthermore, the SHG signal remains active and stable at 487 K (Fig. 2d), demonstrating that the crystal retains its non-centrosymmetric structure in the HTP. This confirms that the phase transition occurs between two non-centrosymmetric structures, a finding consistent with the results of our structural analysis.

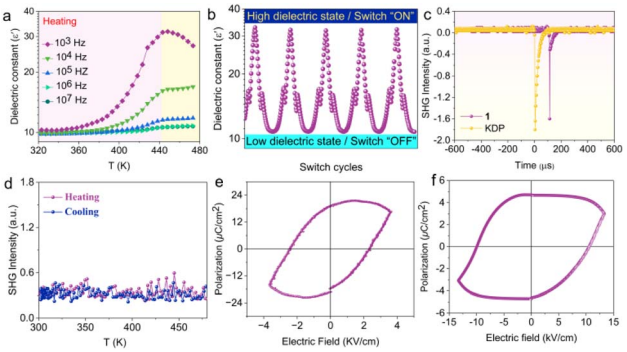

Fig. 2 (a) Temperature-dependent ε' at the selected frequencies upon heating for the polycrystalline sample. (b) The switching dielectric cycles measured at 1 kHz. (c) SHG intensity comparison between KDP and **1** at room temperature. (d) Temperature-dependent SHG intensity of **1** upon heating and cooling. (e) Ferroelectric hysteresis loop of **1** measured for a single crystal using the Sawyer–Tower method at room temperature. (f) Ferroelectric hysteresis loop measured using the double-wave method measured on the powder-pressed pellet at room temperature.

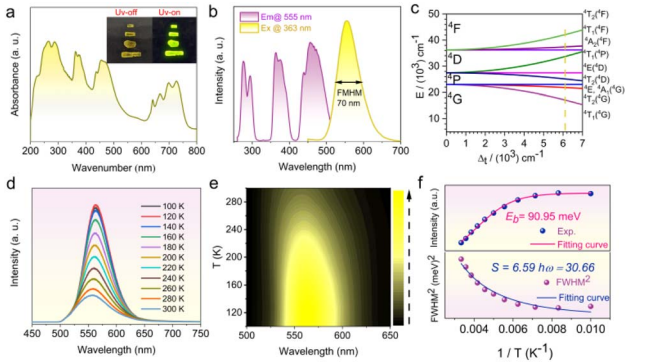

Fig. 3 (a) UV/vis absorption spectra (inset: photographs of single crystals of **1** under ambient light and 365 nm UV lamp irradiation), and (b) normalized PLE and PL spectra of **1** recorded at room temperature. (c) Qualitative energy level diagram of Mn^{2+} ion in $[MnBr_4]^{2-}$ tetrahedral crystal field. (d) Temperature-dependent PL spectra of **1** from 300 to 80 K. (e) Contour plot of the temperature-dependent emission spectra. (f) Temperature-dependent PL intensity and the variation of $FWHM^2$ as a function of $1/T$ and their fitting results, respectively.

Given that both the low-temperature ($P2_1$) and high-temperature ($P3c1$) phases belong to polar space groups, we investigated the ferroelectric properties by measuring polarization–electric field (P–E) hysteresis loops using both the Sawyer–Tower and double-wave methods. Using the Sawyer–Tower method on a single crystal of **1** at room temperature, we observed a well-defined ferroelectric hysteresis loop (Fig. 2e). Notably, **1** possesses a large saturation polarization (P_s) up to around 21.5 μC cm^{-2}, which is close to the calculated value (23.62 μC cm^{-2}) depending on the point charge model (see SI). Remarkably, this P_s value is larger than those of most reported organic–inorganic hybrid ferroelectrics, such as $[Me_3NCH_2CH_2OH]CdCl_3$ (17.1 μC cm^{-2}),[27] $(4,4\text{-difluoropiperidinium})_2GeBr_4$ (15.58 μC cm^{-2}),[28] $(AMP)_2SbBr_5$ (11.28 μC cm^{-2}),[29] and very close to that of perovskite $DMAGeI_3$ (24.14 μC cm^{-2}),[30] also comparable to $BaTiO_3$ (26 μC cm^{-2}).[31] This notable polarization value is attributed to the heavy structure distortion of the $[MnBr_4]^{2-}$ tetrahedra and the relative displacement polarization between the anions and cations. For the double-wave method, a powder-pressed pellet sample of **1** was measured at room temperature. As shown in Fig. 2f, a typical P–E hysteresis loop was observed, directly confirming ferroelectricity. The polarization (P_s) of the powdered sample, measured at approximately 4.7 μC cm^{-2}, is significantly smaller than that of the single crystal. This reduction is attributed to the random orientation of grains of the polycrystalline state of this uniaxial ferroelectric.

Switchable photoluminescence

The crystals of compound **1** are dark yellow under ambient light and exhibit bright yellow photoluminescence (PL) when irradiated with 365 nm ultraviolet (UV) light at room temperature (Fig. 3a). To understand this emission, we collected UV-visible (UV-vis) absorption, photoluminescence excitation (PLE), and PL spectra in the solid state. The UV-vis absorption spectrum of **1** at room temperature shows prominent bands from 230 to 800 nm, characteristic of d–d transitions in Mn^{2+} ions (Fig. 3a). The dark-yellow color arises because the absorption bands between 550 and 800 nm are significantly weaker than those between 230 and 550 nm. Due to the low symmetry of the $[MnBr_4]^{2-}$ tetrahedra, the degenerate excited states split, giving rise to a series of peaks in the UV-vis and PLE spectra at approximately 267, 285, 362, 374, 437, 456, and 471 nm. These correspond to transitions from the $^6A_1(S)$ ground state to higher-energy states ($^4A_2(F)$, $^4T_1(F)$, $^4T_1(P)$, $^4E(D)$, $^4A_1/^4E(G)$, $^4T_2(G)$, and $^4T_1(G)$) of the tetrahedrally coordinated Mn^{2+} ions.[32,33]

Upon 365 nm excitation, the PL spectrum at room temperature shows a single broad band centered at 555 nm with a full width at half maximum (FWHM) of 70 nm. The PLE spectrum monitored at 555 nm matches the absorption features in the 200–500 nm range (Fig. 3b). The emission peak position is independent of the excitation wavelength, and the intensity variation aligns with the PLE spectrum (Fig. S13). The room-temperature PL quantum yield (PLQY) is approximately 30.6%, and the emission decay lifetime at 555 nm is 0.12 ms, as determined by a monoexponential fit (Fig. S14). These results confirm that the yellow emission originates from the d–d transition of Mn^{2+} ions within the $[MnBr_4]^{2-}$ tetrahedron.

Typically, tetrahedrally coordinated Mn-based halides exhibit narrow green emission near 520 nm when Mn···Mn distances are large.[34] However, the emission energy in hybrid Mn(II) halides is highly tunable and depends on several factors, including the Mn^{2+} coordination geometry, polyhedral distortion,[35] Mn···Mn distances,[36,37] intermolecular hydrogen bonds,[38] and halide composition (Br/Cl).[39] These factors alter the ligand field, thereby influencing the emission wavelength and bandwidth.[40] In compound **1**, the nearest Mn···Mn distance increases only slightly from 6.803 Å (LTP) to 6.821 Å (HTP). This minimal change is insufficient to significantly alter the crystal field. Instead, the observed blue shift of the emission band (from 555 nm at LTP to 526 nm at HTP) is attributed to

increased tetrahedral distortion. A greater distortion index enhances the crystal field strength, leading to a larger splitting of the Mn^{2+} 3d levels.[41–43] The Tanabe–Sugano (T–S) diagram for a tetrahedral d^5 Mn^{2+} ion is shown in Fig. 3c. For compound **1**, the tetrahedral crystal field splitting (Δt) was calculated from the PLE spectrum to be 6173 cm^{-1} for LTP (see SI for details).

We further investigated the temperature-dependent PL properties of **1** from 100 K to 473 K (Fig. 3d, e and 4a). A single broad emission band is observed across this entire range. As the temperature increases, the PL intensity gradually decreases due to enhanced non-radiative recombination (Fig. 3d).[44,45] The emission peak shows a minimal blue-shift, moving from 561 nm at 100 K to 558 nm at 300 K (a shift of ~3 nm). The exciton binding energy (E_b) and the Huang–Rhys factor (S), which quantifies electron–phonon coupling, were calculated by fitting the temperature-dependent PL intensity and FWHM using the following equations:[46]

$$I(T) = \frac{I_0}{1 + A\, e^{-\frac{E_b}{k_B T}}} \quad (3)$$

$$\mathrm{FWHM} = 2.36\sqrt{S}\hbar\omega_{\mathrm{phonon}}\sqrt{\coth\frac{\hbar\omega_{\mathrm{phonon}}}{2k_B T}} \quad (4)$$

In eqn (3), $I(T)$ and I_0 represent the integrated emission intensities at different temperatures (T) and 0 K, respectively. A denotes a constant, k_B is the Boltzmann constant, and E_b is the binding energy of an exciton, which is linked to the ability of a material to overcome thermal quenching effects. In eqn (4), S represents the Huang–Rhys factor, $\hbar\omega_{\mathrm{phonon}}$ denotes the phonon frequency, and k_B is the Boltzmann constant. S is generally used to quantify the electron–phonon coupling strength to judge whether it belongs to the self-trapped state (STE) luminescence mechanism. The E_b of compound **1** is determined to be 90.95 meV and the calculated S and phonon energy $\hbar\omega_{\mathrm{phonon}}$ are 6.59 and 30.66 meV, respectively, as illustrated in Fig. 3f. The small S value indicates that the electron–phonon coupling has little effect on the luminescence emission of the sample. So, there is almost no STE involved in the emissions of **1**.[47] Therefore, we conclusively attribute the yellow PL emission of **1** to the d–d transition of Mn^{2+} within the $[MnBr_4]^{2-}$ tetrahedron.

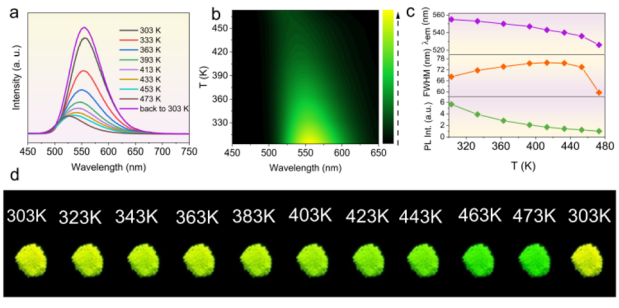

Fig. 4 (a) The temperature-dependent PL spectra of **1** in the range of 303–473 K. (b) Contour plot of the temperature-dependent PL spectra. (c) The comparison of PL peak positions, FWHM and integrated PL intensity as a function of temperature for **1**. (d) The temperature-dependent color changes of **1** under 365 nm UV light.

Fig. 4a–c presents the evolution of the emission spectra from 303 to 473 K, including contour mappings and the variations in peak position, FWHM, and integrated PL intensity with temperature. As the temperature increases from 303 K to 473 K, the emission band undergoes a significant blue-shift of 29 nm, from 555 nm to 526 nm. Concurrently, the PL intensity decreases dramatically, falling to only 17.7% of its initial value at 473 K. The spectrum at this highest temperature exhibits a narrow green emission band centered at 526 nm with an FWHM of 59 nm. Notably, upon cooling back to 303 K, the PL intensity recovers and even surpasses its original level. This behavior is likely caused by the annealing process, which eliminates crystal defects and leads to a more stable state. This interpretation is supported by DSC data (Fig. S3b), where the endothermic peak shifts from 438 K in the first cycle to 428 K in subsequent heating–cooling cycles, a decrease of 10 K. The FWHM shows a monotonic increase up to the phase transition temperature. The visual change in luminescence is captured in Fig. 4d, which shows optical images under 365 nm UV light. The yellow emission intensity declines as the temperature rises from 303 K to 423 K. Near the phase transition temperature, the color changes distinctly to green. The sample instantaneously reverts to its original yellow-emitting state when cooled back to 303 K. This thermochromism is attributed to a structural phase transition. Mn^{2+} ions in a weakly distorted tetrahedral environment typically exhibit green emission. Upon transitioning from the LTP to the HTP, the distortions of the $[MnBr_4]^{2-}$ tetrahedra are reduced, primarily through changes in the Br–Mn–Br bond angles. This reduction in distortion weakens the crystal field strength, resulting in a blue-shift of the emission to green.

Chiroptical properties and their applications for LED

Given the Sohncke space group of the crystal, we investigated its chiroptical properties using circular dichroism (CD) and circularly polarized luminescence (CPL) spectroscopy. The CD spectra exhibit clear mirror-image signals between 200 and 500 nm (Fig. 5a). The pronounced CD activity in this region

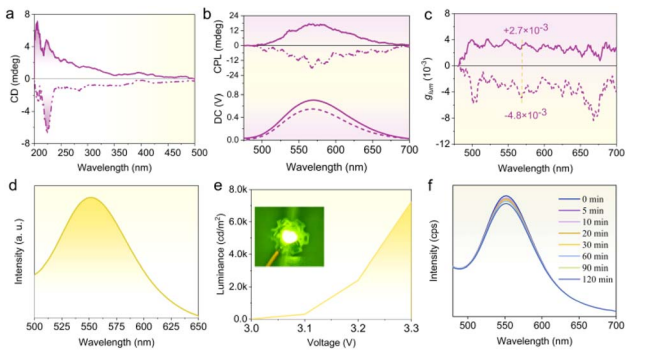

Fig. 5 (a) CD absorption spectra of enantiomers of **1**. (b) CPL spectra of crystal samples excited by 365 nm. (c) The g_{lum} *vs.* wavelength curves of crystal samples. (d) Electroluminescence spectrum of the LED fabricated using a powdered sample of **1** deposited on a 365 nm UV chip. (e) The electroluminescent spectra of the fabricated LED at different voltages of driving. (f) Time-dependent electroluminescent spectra of the LED operated under 3.3 V driving voltage.

indicates that the $[MnBr_4]^{2-}$ tetrahedra act as chiral centres, confirming the successful transfer of chirality from the organic cations to the inorganic moieties through H···Br interactions during self-assembly.

The chiral nature of the excited states was probed by CPL. Crystals of **1** show mirror-image CPL signals in the yellow region (500–700 nm), with peaks at 570 nm and 566 nm (Fig. 5b). These signals correspond to the $^4T_1$–$^6A_1$ transition of the $[MnBr_4]^{2-}$ tetrahedra, consistent with the PL spectrum. The strength of the CPL is quantified by the luminescence dissymmetry factor (g_{lum}), calculated as $g_{lum} = 2 \times (I_L - I_R)/(I_L + I_R)$, where I_L and I_R are the intensities of left- and right-handed CPL, respectively. The calculated g_{lum} values are $+2.7 \times 10^{-3}$ at 570 nm and 4.8×10^{-3} at 566 nm (Fig. 5c). We attribute these chiroptical activities to a synergistic effect: the intrinsic noncentrosymmetry of the $[MnBr_4]^{2-}$ tetrahedra, combined with abundant non-covalent interactions in the crystal lattice, breaks the tetrahedral symmetry and generates the observed CD and CPL signals.[48]

To further validate the potential of the material as lighting emitters, a UV-emitting LED device was fabricated by coating the grounded single-crystal powder onto a commercial UV-LED chip (365 nm, 3 W) and using epoxy encapsulation for protection. The as-fabricated LEDs emit bright and uniform yellow light, and the representative electroluminescent spectrum contains a broad emission band at 553 nm, consistent with the PL spectrum (Fig. 5d). The electroluminescent intensity increases gradually with increasing the driving voltage from 2.0 to 3.3 V (Fig. S15a). At 3.3 V, the luminance remarkably reached 7238 cd m^{-2} (Fig. 5e). Additionally, time-dependent electroluminescent spectra of the as-fabricated LED show excellent device stability, which remains at 93% of the original value after being continuously operated for 2 hours under 3.3 V driving voltage (Fig. 5f). Furthermore, CIE coordinates of (0.35, 0.40) correspond well to the yellow light, as shown in Fig. S17b.

Conclusions

In this study, we demonstrate a crystal engineering strategy to construct NCS structures from achiral molecular building blocks. We successfully synthesized a polar $[MnBr_4]^{2-}$-based hybrid crystal that adopts the polar space group $P2_1$ at room temperature. Upon heating to *ca.* 438 K, this crystal undergoes a structural phase transition to another polar phase (space group $P3c1$), driven by the rotational motion of the organic cations and a synergistic displacement of the $[MnBr_4]^{2-}$ anions. The hybrid crystal exhibits multifunctional properties, including switchable dielectric behavior, the SHG effect, ferroelectricity, reversible thermochromic luminescence, and CPL activity. Both the switchable dielectric response and the thermochromic luminescence are directly linked to the structural phase transition. Our work highlights an effective approach to designing NCS crystalline materials with promising applications in high-tech fields such as ferroelectrics, second-order nonlinear optics, and circularly polarized luminescence, all derived from achiral molecular precursors.

Author contributions

The manuscript was written through contributions of all authors. All authors have given approval to the final version of the manuscript.

Conflicts of interest

There are no conflicts to declare.

Data availability

CCDC 2467490 [for **1** at 298 K (LTP)] and 2467491 [for **1** at 438 K (HTP)] contain the supplementary crystallographic data for this paper.[49a,b]

The data supporting this article have been included as part of the supplementary information (SI). Supplementary information: experimental details, structural and computational details, IR, TG, DSC, PXRD, PL, CPL and electroluminescence spectra. See DOI: https://doi.org/10.1039/d5sc08499g.

Acknowledgements

Authors thank the Priority Academic Program Development of Jiangsu Higher Education Institutions and National Nature Science Foundation of China (grant no. 22073047 and 21901116) for financial support. W. N. acknowledges support from the Suzhou Key Laboratory of Functional Nano & Soft Materials, the Collaborative Innovation Centre of Suzhou Nano Science & Technology, the 111 Project, the Joint International Research Laboratory of Carbon-Based Functional Materials and Devices (Z221311), and the Gusu Innovation and Entrepreneurship Leading Talent Program (ZXL2023188).

Notes and references

1 B.-W. Deng, Y. Zhu, K. Ding, J. Li, M.-M. Lun, D.-W. Fu and Z.-X. Zhang, *Inorg. Chem.*, 2023, **62**, 11701.
2 M.-E. Sun, Y. Wang, F. Wang, J. Feng, L. Wang, H. Gao, G. Chen, J. Gu, Y. Fu, K. Bu, T. Fu, J. Li, X. Lü, L. Jiang, Y. Wu and S.-Q. Zang, *J. Am. Chem. Soc.*, 2023, **145**, 8908.
3 L. Hua, J. Wang, Y. Liu, W. Guo, Y. Ma, H. Xu, S. Han, J. Luo and Z. Sun, *Adv. Sci.*, 2023, **10**, 2301064.
4 Q.-Q. Jia, H.-F. Lu, J.-Q. Luo, Y.-Y. Zhang, H.-F. Ni, F.-W. Zhang, J. Wang, D.-W. Fu, C.-F. Wang and Y. Zhang, *Small*, 2024, **20**, 2306989.
5 H. Xu, W. Guo, Y. Liu, Y. Ma, Q. Fan, L. Tang, W. Li, H. Ni, J. Luo and Z. Sun, *Angew. Chem.*, 2025, **137**, e202501238.
6 H. Zheng, A. Ghosh, M. J. Swamynadhan, Q. Zhang, W. P. D. Wong, Z. Wu, R. Zhang, J. Chen, F. Cimpoesu, S. Ghosh, B. J. Campbell, K. Wang, A. Stroppa, R. Mahendiran and K. P. Loh, *Nat. Commun.*, 2024, **15**, 5556.
7 Z. Sun, T. Chen, X. Liu, M. Hong and J. Luo, *J. Am. Chem. Soc.*, 2015, **137**, 15660.
8 M.-L. Jin, X.-B. Han, C.-D. Liu, B.-D. Liang, C.-Q. Jing, W. Wang, C.-C. Fan, T.-Y. Ju, J.-M. Zhang and W. Zhang, *Adv. Funct. Mater.*, 2024, **34**, 2408120.

9 S. Lin, G. Zhang, Q. Lai, J. Fu, W. Zhu and H. Zeng, *Adv. Funct. Mater.*, 2023, **33**, 2304139.
10 L. Du, Q. Zhou, Q. He, Y. Liu, Y. Shen, H. Lv, L. Sheng, T. Cheng, H. Yang, L. Wan, Y. Fang and W. Ning, *Adv. Funct. Mater.*, 2024, **34**, 2315676.
11 J.-X. Gao, W.-Y. Zhang, Z.-G. Wu, Y.-X. Zheng and D.-W. Fu, *J. Am. Chem. Soc.*, 2020, **142**, 4756.
12 M.-L. Jin, X.-B. Han, C.-D. Liu, B.-D. Liang, C.-Q. Jing, W. Wang, C.-C. Fan, T.-Y. Ju, J.-M. Zhang and W. Zhang, *Adv. Funct. Mater.*, 2024, **34**, 2408120.
13 H. Y. Zhang, Y. Y. Tang, P. P. Shi and R. G. Xiong, *Acc. Chem. Res.*, 2019, **52**, 1928.
14 R.-G. Xiong, S.-Q. Lu, Z.-X. Zhang, H. Cheng, P.-F. Li and W.-Q. Liao, *Angew. Chem., Int. Ed.*, 2020, **59**, 9574.
15 J. Zhao, T. Zhang, X.-Y. Dong, M.-E. Sun, C. Zhang, X. Li, Y. S. Zhao and S.-Q. Zang, *J. Am. Chem. Soc.*, 2019, **141**, 15755.
16 K. M. Ok, *Acc. Chem. Res.*, 2016, **49**, 2774.
17 C. Wang, T. Zhang and W. Lin, *Chem. Rev.*, 2012, **112**, 1084.
18 V. Jornet-Mollá, Y. Duan, C. Giménez-Saiz, Y. Y. Tang, P. F. Li, F. M. Romero and R. G. Xiong, *Angew. Chem., Int. Ed.*, 2017, **56**, 14052.
19 H.-Y. Liu, H.-Y. Zhang, X.-G. Chen and R.-G. Xiong, *J. Am. Chem. Soc.*, 2020, **142**(36), 15205.
20 E. D. Sødahl, S. Seyedraoufi, C. H. Görbitz and K. Berland, *Cryst. Growth Des.*, 2023, **23**, 8607.
21 Y. Ai, X.-G. Chen, P.-P. Shi, Y.-Y. Tang, P.-F. Li, W.-Q. Liao and R.-G. Xiong, *J. Am. Chem. Soc.*, 2019, **141**, 4474.
22 L. Zhai, J. Yuan, J. Huang, X.-W. Pan, L. Wan, W. Ning and X.-M. Ren, *Angew. Chem., Int. Ed.*, 2025, **64**, e202425543.
23 K. Robinson, G. V. Gibbs and P. H. Ribbe, *Science*, 1971, **172**, 567.
24 N. Chakraborty, T. A. Ngo, A. D. Montero, T. Liyanage, G. T. McCandless, J. Y. Chan, T. D. Nguyen and L. Whittaker-Brooks, *J. Am. Chem. Soc.*, 2025, **147**, 29431.
25 D. Jayatilaka, S. K. Wolff, D. J. Grimwood, J. J. McKinnon and M. A. Spackman, *Acta Crystallogr., Sect. A:Found. Crystallogr.*, 2006, **62**, S90.
26 M.-L. Jin, X.-B. Han, C.-D. Liu, C.-Y. Chai, C.-Q. Jing, W. Wang, C.-C. Fan, J.-M. Zhang and W. Zhang, *J. Am. Chem. Soc.*, 2024, **146**(9), 6336.
27 S. Deswal, S. K. Singh, R. Pandey, P. Nasa, D. Kabra, B. Praveenkumar, S. Ogale and R. Boomishankar, *Chem. Mater.*, 2020, **32**(19), 8333.
28 H.-F. Ni, Q.-F. Zhou, J.-Q. Luo, G. Teri, L. Pan, L.-K. Ye, Q.-Q. Jia, P.-Z. Huang, P.-G. Liu, C.-F. Wang, Z.-X. Zhang, D.-W. Fu and Y. Zhang, *Nat. Commun.*, 2025, **16**, 7760.
29 B. Zhuang, L. Pan, Z.-L. Li, J.-Y. Liu, Z.-X. Zhang, K. Ding, Y. Zhang, Z. Liu and D.-W. Fu, *ACS Mater. Lett.*, 2025, **7**, 1540.
30 K. Ding, H. Ye, C. Su, Y.-A. Xiong, G. Du, Y.-M. You, Z.-X. Zhang, S. Dong, Y. Zhang and D.-W. Fu, *Nat. Commun.*, 2023, **14**, 2863.
31 S. Horiuchi and Y. Tokura, *Nat. Mater.*, 2008, **7**, 357.
32 Y.-H. Liu, Y.-F. Wu, L.-J. Feng, R.-R. Zhao, S.-X. Wang, M. Zhang, D.-Y. Wang, X.-W. Kong and X.-W. Lei, *Chem. Commun.*, 2023, **59**, 10267.
33 J. Zhang, X. Wang, W.-Q. Wang, X. Deng, C.-Y. Yue, X.-W. Lei and Z. Gong, *Inorg. Chem.*, 2024, **63**, 2647.
34 M. Li, J. Zhou, M. S. Molokeev, X. Jiang, Z. Lin, J. Zhao and Z. Xia, *Inorg. Chem.*, 2019, **58**, 13464.
35 G. Zhou, J. Ding, X. Jiang, J. Zhang, M. S. Molokeev, Q. Ren, J. Zhou, S. Lia and X.-M. Zhang, *J. Mater. Chem. C*, 2022, **10**, 2095.
36 V. Morad, I. Cherniukh, L. Pöttschacher, Y. Shynkarenko, S. Yakunin and M. V. Kovalenko, *Chem. Mater.*, 2019, **31**, 10161.
37 T. Huang, Q. Wei, W. Lin, H. Peng, S. Yao and B. Zou, *Mater. Today Phys.*, 2022, **25**, 100703.
38 J. Lin, M. Zhang, N. Sun, S. He, X. Zhang, Z. Guo, J. Zhao, Q. Liu and W. Yuan, *J. Mater. Chem. C*, 2022, **10**, 16773.
39 D. Wang, H. Dong, L. Zhang, D. Wu, L. Ren, D. Zhao, T. Wang and M. Feng, *Laser Photonics Rev.*, 2025, 2401982.
40 Z. Qi, K. Zhang, X. Zhao, N. Zhang, S.-L. Lia and X.-M. Zhang, *Chem. Commun.*, 2024, **60**, 12880.
41 K. A. Denault, J. Brgoch, M. W. Gaultois, A. Mikhailovsky, R. Petry, H. Winkler, S. P. DenBaars and R. Seshadri, *Chem. Mater.*, 2014, **26**, 2275.
42 Z. H. Leng, R. F. Li, L. P. Li, D. K. Xue, D. Zhang, G. S. Li, X. Y. Chen and Y. Zhang, *ACS Appl. Mater. Interfaces*, 2018, **10**, 33322.
43 Z. Q. Ming, J. W. Qiao, M. S. Molokeev, J. Zhao, H. C. Swart and Z. G. Xia, *Inorg. Chem.*, 2020, **59**, 1405.
44 A. J. V. Bunningen, A. D. Sontakke, R. V. D. Vliet, V. G. Spit and A. Meijerink, *Adv. Opt. Mater.*, 2023, **11**, 2202794.
45 Y. Xiao, Z. Xie, M. Shen, H. Wang, J. Li, R. Huang and T. Yu, *FlexMat*, 2024, **1**, 258.
46 R. Zeng, L. Zhang, Y. Xue, B. Ke, Z. Zhao, D. Huang, Q. Wei, W. Zhou and B. Zou, *J. Phys. Chem. Lett.*, 2020, **11**, 2053.
47 Y. Han, J. Yin, G. Cao, Z. Yin, Y. Dong, R. Chen, Y. Zhang, N. Li, S. Jin, O. F. Mohammed, B. B. Cui and Q. Chen, *ACS Energy Lett.*, 2022, **7**, 453.
48 C. Li, Y. Wei, Y. Li, Z. Luo, Y. Liu, M. He, Y. Zhang, X. He, X. Chang and Z. Quan, *Small*, 2024, **20**, 2400338.
49 (*a*) CCDC 2467490: Experimental Crystal Structure Determination, 2026, DOI: 10.5517/ccdc.csd.cc2ntmgl; (*b*) CCDC 2467491: Experimental Crystal Structure Determination, 2026, DOI: 10.5517/ccdc.csd.cc2ntmhm.